Available online at www.sciencedirect.com
SCIENCE DIRECT®

Journal of Catalysis 235 (2005) 279–294

JOURNAL OF CATALYSIS

www.elsevier.com/locate/jcat

$La_{(1-y)}Co_{0.4}Fe_{0.6}O_{3-\delta}$ perovskite oxides as catalysts for Fischer–Tropsch synthesis

Laurent Bedel [a], Anne-Cécile Roger [a,*], Jean-Luc Rehspringer [b], Yvan Zimmermann [a], Alain Kiennemann [a]

[a] *Laboratoire des Matériaux, Surfaces et Procédés pour la Catalyse, ECPM, UMR 7515, 25 rue Becquerel, 67087 Strasbourg cedex 2, France*
[b] *Groupe des Matériaux Inorganiques, Equipe Matériaux et Applications, IPCMS, UMR 7504, 23 rue du Loess, BP 43, 67034 Strasbourg cedex 2, France*

Received 17 June 2005; revised 27 July 2005; accepted 29 July 2005

Abstract

A previous study of $LaCo_xFe_{(1-x)}O_3$ perovskites demonstrated the potential of such materials to produce light olefins from syngas by Fischer–Tropsch synthesis. The partial reduction of $LaCo_{0.4}Fe_{0.6}O_3$ generates small Co^0 particles in interaction with a deficient perovskite. However, the stability of the perovskite limits the amount of metal to 2% in weight. To increase the amount of active phase (metal) that can be extracted from the oxide precursor by reduction, we attempted to synthesize A-site deficient perovskites. $La_{(1-y)}Co_{0.4}Fe_{0.6}O_{3-\delta}$ series prepared by a sol–gel-like route revealed to be, instead of expected A-site deficient oxides, γ-Fe_2O_3/$LaCo_zFe_{(1-z)}O_3$ composites. Magnetic nanocores of γ-Fe_2O_3 are surrounded by a perovskite-type shell. The epitaxial growth of the perovskite phase on the cubic iron oxides drives its crystallization toward the same cubic system. The characterization of $La_{(1-y)}Co_{0.4}Fe_{0.6}O_{3-\delta}$ oxides are presented, and the structural hypotheses are discussed. The reducibility of such oxides is studied by thermoprogrammed reduction and Mössbauer experiments, and the formulae of the stable partially reduced materials are determined. These materials are composed of an equimolar Co–Fe alloy on a cubic perovskite enriched in iron with respect to that of the fresh catalyst. The γ-Fe_2O_3 disappear; one part of the Fe^{3+} cations is reduced into Fe^0 in the alloy, and the other part of the Fe^{3+} "replaces" a part of the Co^{3+} cations of the perovskite, which also reduce into Co^0 in the alloy. After partial reduction, the reactivity of these oxides in Fischer–Tropsch synthesis is evaluated. Their efficiency to produce light olefins and their stability over 300 h of test is demonstrated.

Keywords: Perovskite; Composite; Fischer–Tropsch; Light olefins

1. Introduction

Perovskites have been of major interest over the past decades because of their numerous applications [1,2]. For example, the oxygen-permeating property of $LaSrBFeO_3$ ($B = Co$, Ga) perovskite makes it suitable as membrane [3], whereas interest in the $La_{1-x}Ca_xMnO_3$ series is because of its magnetic properties [4]. Perovskites are also widely studied in the heterogeneous catalysis field, particularly for oxidation reactions, such as total [5–8] or partial [9,10] methane oxidation. In addition, they can be partially reduced to generate metal particles within stable cation-deficient perovskite [11,12].

Because Co and Fe are the most widely adapted metal catalysts for Fischer–Tropsch synthesis, we integrated both metals in a La-based perovskite to obtain, after partial reduction, efficient catalysts for light olefin formation from syngas. Earlier studies on the $LaCo_xFe_{(1-x)}O_3$ series [12] have pointed out that the amount of extractable metal is closely related to both the perovskite crystalline system (only orthorhombic perovskites [$x < 0.5$] enable metal formation after partial reduction) and the calcination temperature. When calcined at 750 °C, the maximum extractable metal amount reaches 2.1 wt% for $LaCo_{0.4}Fe_{0.6}O_3$. Metal formation is limited by the very high stability of the perovskite. To improve it, the perovskite crystalline structure must be weakened. The challenge was to introduce A-site vacancies in the ABO_3 perovskite structure to

---

[*] Corresponding author. Fax: +33 3 90 24 27 68.
E-mail addresses: rogerac@ecpm.u-strasbg.fr (A.-C. Roger), kiennemann@ecpm.u-strasbg.fr (A. Kiennemann).

0021-9517/$ – see front matter © 2005 Elsevier Inc. All rights reserved.
doi:10.1016/j.jcat.2005.07.025

decrease its stability, as well as increase the amount of reducible B-cations.

The literature contains numerous reports of deficient perovskites [13–18]. For instance, Stevenson et al. [13] studied $(La_{1-x}Sr_x)_{1-\varepsilon}(Ga_{0.8}Mg_{0.2})O_{3-\delta}$ materials, and Waller et al. [14] reported the existence of a 27% A-site deficient perovskite phase, $(La_{0.6}Sr_{0.13})(Co_{0.2}Fe_{0.8})O_{3-\delta}$.

This paper presents the materials of the general formula $La_{(1-y)}Co_{0.4}Fe_{0.6}O_{3-\delta}$ and discusses the advanced characterics of the structure. It also describes the reducibility of the lanthanum-deficient perovskites and discusses their efficiency as catalysts for Fischer–Tropsch reactions to produce light olefins.

2. Experimental

2.1. Preparation of fresh catalysts

The $La_{(1-y)}Co_{0.4}Fe_{0.6}O_{3-\delta}$ oxides (for y between 0 and 0.4) were prepared by a soft chemistry method based on the thermal decomposition of mixed La–Co–Fe propionates [19]. Starting materials [powdered Fe^0, La acetate $La(OOCCH_3)_3 \cdot 1.5H_2O$, and Co acetate $Co(OOCCH_3)_2 \cdot 4H_2O$] were separately dissolved in boiling propionic acid at a concentration of 3×10^{-3} mol L^{-1} in cations. Each starting salt leads to the exclusive formation of the corresponding propionates (controlled by IR of the species crystallized from the propionate solution) [19,20]. The three boiling solutions were then mixed to generate mixed La–Co–Fe propionates in solution, and, after 30 min of stirring, propionic acid was evaporated until a dark-brown pasty resin was obtained. The final oxide resulted from 6 h of calcination of the resin at either 750 or 900 °C (2 °C min^{-1}).

2.2. Characterization

X-Ray diffraction (XRD) was done recorded using a Siemens D5000 diffractometer equipped with a Co-K_α source. Patterns were recorded between 20, and 85° (2θ scale) with 0.04° steps and a 5-s counting time.

^{57}Fe Mössbauer spectra were recorded using a spectrometer equipped with a 50 mCi ^{57}Co in Rh source. A bath cryostat allowed measurements for all samples at a liquid He temperature of 4 K. The spectrometer was calibrated with reference to a sheet of α-Fe, and isomer shift values are given relative to this.

The magnetic properties were studied on a Föner VSM magnetometer in the 300 to 4 K temperature range and under a maximum magnetic field of 18,000 Oe.

Materials morphology was studied using a Topcon EM-002B transmission microscope coupled to a Kevex Deltapro Quantum EDX spectrometer.

Thermoprogrammed reductions (TPRs) were carried out on 50 mg of catalyst, heated from 25 to 900 °C (15 °C min^{-1}) under 10% H_2/He (total gas flow, 50 mL min^{-1}). The hydrogen consumption was followed and quantified by an external standard.

2.3. Catalytic tests

For the reaction of CO dissociation, 100 mg of catalyst was first reduced in situ by heating from 20 to 450 °C (2 °C min^{-1}) under a 10% H_2/He flow (total gas flow, 50 mL min^{-1}). The flow was then replaced by only He at 30 mL min^{-1}. At 350 °C, pulses of CO (0.5 mL) were admitted onto the catalyst at steady 8-min intervals. The exit gases (CO and CO_2) were analyzed by gas chromatography.

Catalytic tests under CO/H_2 were performed in a fixed-bed reactor at 1 MPa pressure. First, 300 mg of catalyst was reduced in situ under 10% H_2/He. The reduced catalyst was then heated under N_2, which was then replaced by the CO/H_2 (1:1) mixture with a GHSV of 3000 h^{-1}. The catalytic tests were carried out between 210 and 280 °C, for 50 h at each temperature. The reaction products were analyzed on-line by gas chromatography.

3. Results and discussion

3.1. Characterization of fresh catalysts

3.1.1. Bulk analysis and specific surface areas

The $La_{(1-y)}Co_{0.4}Fe_{0.6}O_{3-\delta}$ oxides ($y = 0$, 0.1, 0.2, 0.3, and 0.4) are black powders. Their exact composition, reported in Table 1, was determined by ICP. Because of greater than expected hydration of lanthanum acetate, lanthanum deficiency was generally greater than expected (e.g., $y = 0.43$ instead of 0.40). Despite this difference, the samples are labeled based on their theoretical lanthanum deficiency.

For the series at 750 °C, the specific surface area increased with y (from 6.8 m^2 g^{-1} for $y = 0$ to 10.9 m^2 g^{-1} for $y = 0.4$). For the series at 900 °C, the specific surface area decreased with y (from 4.3 m^2 g^{-1} for $y = 0$ to 2.8 m^2 g^{-1} for $y = 0.4$). In all cases the surfaces were very low, and the variations were not considered significant.

Table 1
$\theta_{\square}$ (dimension of the A-site vacancies) and a' (theoretical cubic cell parameter) calculated parameters according to hypotheses 1, 2 and 3

y	Exact composition	a (Å)		$\theta_{\square}$ (Å) hypothesis 1	a' (Å) hypothesis 2	a' (Å) hypothesis 3
		750 °C	900 °C			
0	$LaCo_{0.4}Fe_{0.6}O_3$	3.912(4)	3.896(4)	–	3.911	3.911
0.1	$La_{0.82}Co_{0.38}Fe_{0.62}O_{3-\delta}$	3.904(4)	3.882(4)	5.35	3.894	3.895
0.2	$La_{0.66}Co_{0.48}Fe_{0.52}O_{3-\delta}$	3.910(3)	3.886(3)	3.90	3.878	3.876
0.3	$La_{0.66}Co_{0.40}Fe_{0.60}O_{3-\delta}$	3.902(3)	3.893(3)	3.88	3.879	3.877
0.4	$La_{0.57}Co_{0.40}Fe_{0.60}O_{3-\delta}$	3.909(3)	3.900(2)	3.52	3.871	3.866

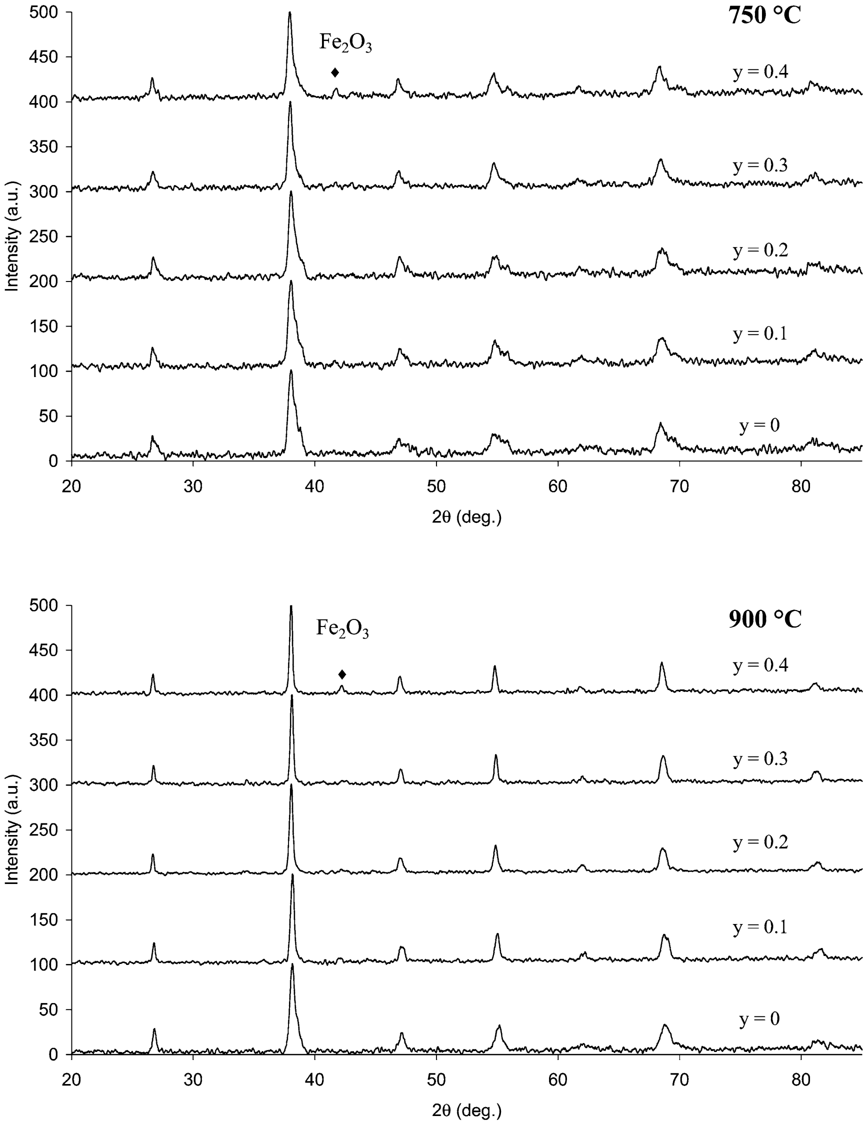

Fig. 1. Diffractograms of $La_{(1-y)}Co_{0.4}Fe_{0.6}O_{3-\delta}$. Calcined at 750 and 900 °C.

3.1.2. XRD

The XRD diffraction patterns of samples calcined at 750 and 900 °C are presented in Fig. 1. For both calcination temperatures, a given sample led to the same observed reflections in the diffractogram. Only the crystallinity was affected by varying the calcination temperature; those at 900 °C exhibited a better signal on noise ratio and narrower lines than those at 750 °C. For La-deficiency $< y = 0.4$, all reflections can be assigned to a single cubic perovskite-type phase, whereas non-La-deficient $LaCo_xFe_{(1-x)}O_3$ oxides crystallized in either the orthorhombic (when $x < 0.5$) or the rhombohedral system (when $x \geqslant 0.5$) [12]. An additional weak reflection was detected at $2\theta = 41.4°$ ($d = 2.53$ Å) for the $y = 0.4$ samples (750 and 900 °C calcined) only. This line may be due to a trace of iron oxide, α- or γ-Fe_2O_3. The nonsymmetric shape of the reflections (especially in calcination at 750 °C) may be due to either the K_{α_2} radiation or a gradient of the perovskite composition. To more easily compare the different patterns, a reflection position was assigned to its maximum intensity. The cubic cell parameter "a" of the perovskite phase was calculated using a least squares method [21]; results are given in Table 1.

Despite an average ionic radius decreasing with the lanthanum content, the cell parameter remained the same within experimental limits (3.902–3.912 Å for calcination at 750 °C and 3.882–3.900 Å for calcination at 900 °C). Furthermore, this very small variation is not linear with the La deficiency. No obvious relation between the cell parameter of the perovskite and its stoichiometry is seen.

Three structural hypotheses can be proposed to describe such La-deficient perovskite single phases. First, considering the work of Chakhmouradian et al. [18] on the $Th_{0.25}\square_{0.75}NbO_3$ system, we can infer that A-site cationic vacancies may be envisaged. Second, B-site cationic vacancies, with fewer constraints, have also been reported [22] and can be considered; third, a combination of the two assumptions is possible. Formulations according to each hypothesis are as follows:

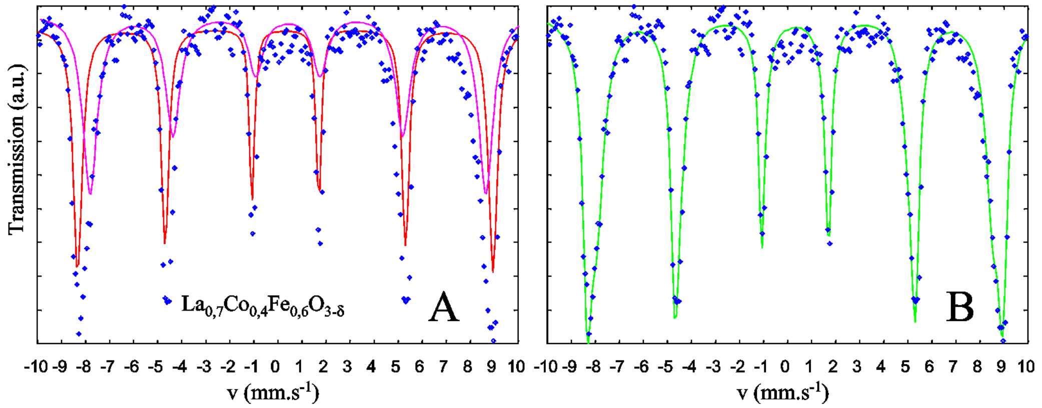

Fig. 2. $La_{0.7}Co_{0.4}Fe_{0.6}O_{3-\delta}$ experimental Mössbauer spectrum at 4 K and its deconvoluted components (A) or their sum (B).

1. A-Site cationic vacancies. The detailed formulation should be:

   $(La_{(1-y)}\square_y)(Co_{0.4}Fe_{0.6})O_{3-\delta}$.

2. B-Site cationic vacancies and presence of Fe in A-sites. Compounds can be written as:

   $(La_{(1-y)}Fe_y)(Co_{0.4}Fe_{0.6-y}\square_y)O_{3-\delta}$.

3. No cationic vacancies and presence of Fe in A-sites. The formulation could be:

   $(La_{(1-y)}Fe_{y/2})(Co_{0.4}Fe_{0.6-y/2})O_{3-\delta}$.

According to hypotheses 2 and 3, we can calculate a theoretical cubic cell parameter, a', using the method of Poix [23] based on the invariance of the cation–oxygen distance. For cubic perovskite, the cell parameter a' can be estimated by the relation

$$1.207a' = \sum_i \nu_i\theta_i + \sum_j \nu_j\beta_j,$$

where $\nu_{i,j}$ are the stoichiometric coefficients and θ_i and β_j are the cation–oxygen distance with 12-fold and 6-fold coordination, respectively. Fe in A-sites is supposed to be Fe^{2+}; 12-fold coordinated Fe^{3+} in oxide is not known.

It is not possible to calculate a theoretical cell parameter in accordance with the first hypothesis, because the dimension of the A-site vacancies $\theta_\square$ is unknown. However, we can estimate this parameter ($\theta_\square$) from the experimental cell parameter. For hypothesis 1 to be true, the calculated $\theta_\square$ must be constant for all samples. Calculated parameters a' and $\theta_\square$ are reported in Table 1.

The hypothetical A-site vacancies exhibited size fluctuations from 5.35 to 3.52 Å; this clearly is not feasible. All of the calculated a' parameters are closely related to the La content of the sample and decrease linearly with it, whereas we observe that the experimental cell parameter was almost constant along the series and obviously independent of the La content. None of the above assumptions are acceptable to describe the $La_{(1-y)}Co_{0.4}Fe_{0.6}O_{3-\delta}$ materials. Further characterizations are therefore required.

Table 2
Characteristics of the $La_{0.7}Co_{0.4}Fe_{0.6}O_{3-\delta}$ deconvoluted Mössbauer components

Component	δ (mm s^{-1})	Δ (mm s^{-1})	H (kG)	Attribution	(%)
Sextet	0.358	0	538	Fe^{3+} (B-site)	42
Sextet	0.349	0	512	Fe_2O_3	58

3.1.3. *Mössbauer*

To precisely determine the degree and location of Fe oxidation, ^{57}Fe Mössbauer spectroscopy was performed. A typical spectrum of the 750 °C calcined $La_{0.7}Co_{0.4}Fe_{0.6}O_{3-\delta}$ sample recorded at 4 K is shown in Fig. 2.

The experimental spectrum was deconvoluted into two sextets, the parameters of which are reported in Table 2. To fit the experimental spectrum, external bands of the first sextet must be broadened by considering a gradient in the hyperfine field. Such enlargement results from variation within the Fe^{3+} environment from changes in either the composition gradient of the phase or the size distribution of the grains. The mean parameters of this sextet were $\delta = 0.358$ mm s^{-1} and $H = 538$ kG. This sextet was assigned to Fe^{3+} located in the perovskite phase B-sites [24,25]. Despite the gradient of the hyperfine field, a second sextet was needed to achieve the fit ($\delta = 0.349$ mm s^{-1}, $H = 512$ kG). This sextet was assigned to Fe^{3+} in an Fe_2O_3 phase [26].

Thus, neither Fe^{2+} nor Fe^{3+} in perovskite A-sites was detected; however, Fe in perovskite B-sites represents only 42% of the total Fe contained in the sample. The crystallized Fe_2O_3 phase present in large amounts in the material (58% of the Fe) was then observable by Mössbauer spectroscopy, but not by XRD (except for $y = 0.4$). The fact that α- and γ-Fe_2O_3 have similar Mössbauer spectra makes exact identification difficult; however, we can speculate that instead of having an A-site deficient perovskite-type phase, the excess B cations were rejected via Fe into the observed Fe_2O_3 phase.

3.1.4. *Magnetic measurements*

The magnetic behaviors of α- and γ-Fe_2O_3 differ. α-Fe_2O_3 is an antiferromagnet below the Morin transition of 243 K and a weak ferromagnet above this transition (maximum magnetization of 0.4 emu g^{-1}) [27]. γ-Fe_2O_3 is ferrimagnetic with a

Table 3
Developed formulation of $La_{(1-y)}Co_{0.4}Fe_{0.6}O_{3-\delta}$

y	Raw formula (ICP determination)	Developed formula	Calculated a' (Å)	a_{exp} (750 °C) (Å)
0	$LaCo_{0.40}Fe_{0.60}O_3$	$[La][Co_{0.40}Fe_{0.60}]O_3$	3.911	3.912(4)
0.1	$La_{0.82}Co_{0.38}Fe_{0.62}O_{3-\delta}$	$[La][Co_{0.46}Fe_{0.54}]O_3 + 0.11Fe_2O_3$	3.910	3.904(4)
0.2	$La_{0.66}Co_{0.48}Fe_{0.52}O_{3-\delta}$	$[La][Co_{0.73}Fe_{0.27}]O_3 + 0.26Fe_2O_3$	3.906	3.910(3)
0.3	$La_{0.66}Co_{0.40}Fe_{0.60}O_{3-\delta}$	$[La][Co_{0.61}Fe_{0.39}]O_3 + 0.26Fe_2O_3$	3.908	3.902(3)
0.4	$La_{0.57}Co_{0.40}Fe_{0.60}O_{3-\delta}$	$[La][Co_{0.70}Fe_{0.30}]O_3 + 0.38Fe_2O_3$	3.906	3.909(3)

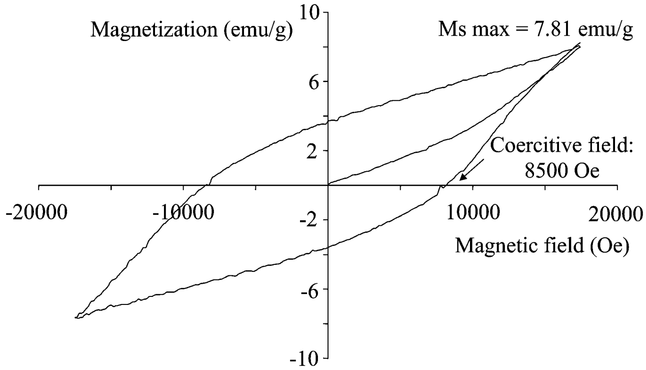

Fig. 3. Virgin magnetization (after ZFC) and hysteresis effect at 4 K for $La_{0.7}Co_{0.4}Fe_{0.6}O_{3-\delta}$ calcined at 750 °C.

maximum magnetization of 74 emu g^{-1} but only 59.2 emu g^{-1} when the particles are small [28]. The magnetic behavior of the $La_{(1-y)}Co_{0.4}Fe_{0.6}O_{3-\delta}$ series was studied to obtain more information about the structure. As shown in Fig. 3 for $La_{0.7}Co_{0.4}Fe_{0.6}O_{3-\delta}$ calcined at 750 °C, a hysteresis cycle was obtained when varying the magnetic field between −18 and +18 kOe. The existence of a strong coercive field (8500 Oe) is consistent with a hard magnetic material.

The observed magnetization of the sample of 7.8 emu g^{-1} cannot be assigned only to the perovskite contribution. Indeed, previous work on pure $LaCo_xFe_{1-x}O_3$ indicated that such oxides present a maximal magnetization of about 1.3 emu g^{-1} [29]. A 6.5 emu g^{-1} contribution of Fe_2O_3 then must be considered to explain the experimental magnetization of 7.8 emu g^{-1}. Such magnetization (6.5 emu g^{-1}) is higher than the theoretical maximum for α-Fe_2O_3 (0.4 emu g^{-1} for pure α-Fe_2O_3) The iron oxide phase cannot be considered α-Fe_2O_3, but if we assign the experimental magnetization to γ-small Fe_2O_3 small particles (59.2 emu g^{-1} theoretical magnetization when small particles), then these particles should represent at least $6.5/59.2 = 11$ wt% of the sample.

If we assume that the perovskite phase has no cation deficiency and that the excess B cations form the γ-Fe_2O_3 phase, then the formulation of the $La_{(1-y)}Co_{0.4}Fe_{0.6}O_{3-\delta}$ oxides can be broken down to $\frac{y}{2}Fe_2O_3 + La_{(1-y)}Co_{0.4}Fe_{(0.6-y)}O_{3-\delta}$. To recover an ABO_3 perovskite, all of the stoichiometric coefficients must be divided by $(1-y)$. The formulation of these materials is summarized in Table 3.

The exact composition of the $y = 0.3$ sample is $La_{0.66}Co_{0.40}Fe_{0.60}O_{3-\delta}$. Taking into account no cation vacancy and presence of an iron oxide phase, this can be broken down into its components, $LaCo_{0.61}Fe_{0.39}O_3 + 0.26Fe_2O_3$. In this composite material, iron oxide represents 10.6 wt% of the sample. This formulation is then in close agreement with the 11 wt% of γ-Fe_2O_3 estimated from magnetization data (Fig. 3). In this formulation, the Fe in Fe_2O_3 represents 57% of the total Fe of the sample, corresponding to the phase repartition calculated from the Mössbauer results (58%, see Table 2).

Thus, like the experimental cell parameters a (see Table 1), the variation of the calculated cell parameters a' along the series was very weak and independent of the La deficiency. This also confirms the assumptions that we made to describe the $La_{(1-y)}Co_{0.4}Fe_{0.6}O_{3-\delta}$ materials.

In our systems, three structures drawing these two-phase oxides can be envisaged, as schematized in Scheme 1. A core-shell phenomenon can be imagined with either a unique γ-Fe_2O_3 core (Scheme 1A) or multiple nanosized-cores dispersed in the perovskite phase (Scheme 1B). The last possibility (Scheme 1C) is that the two phases coexist as individual particles, but with a γ-Fe_2O_3 size too small to diffract X-rays.

3.1.5. *TEM*

Samples were dispersed in a resin, then cut and polished. The cut of 750 °C calcined $La_{0.7}Co_{0.4}Fe_{0.6}O_{3-\delta}$ material ob-

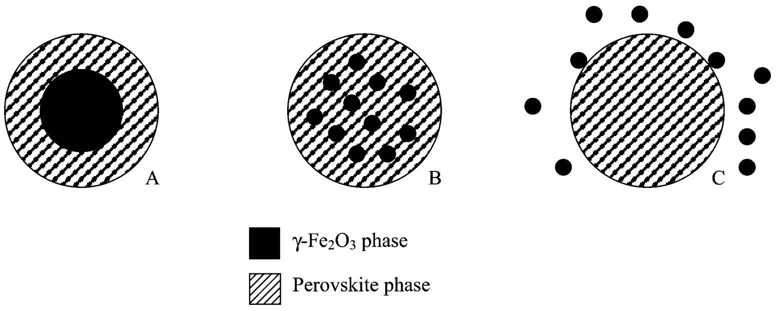

Scheme 1.

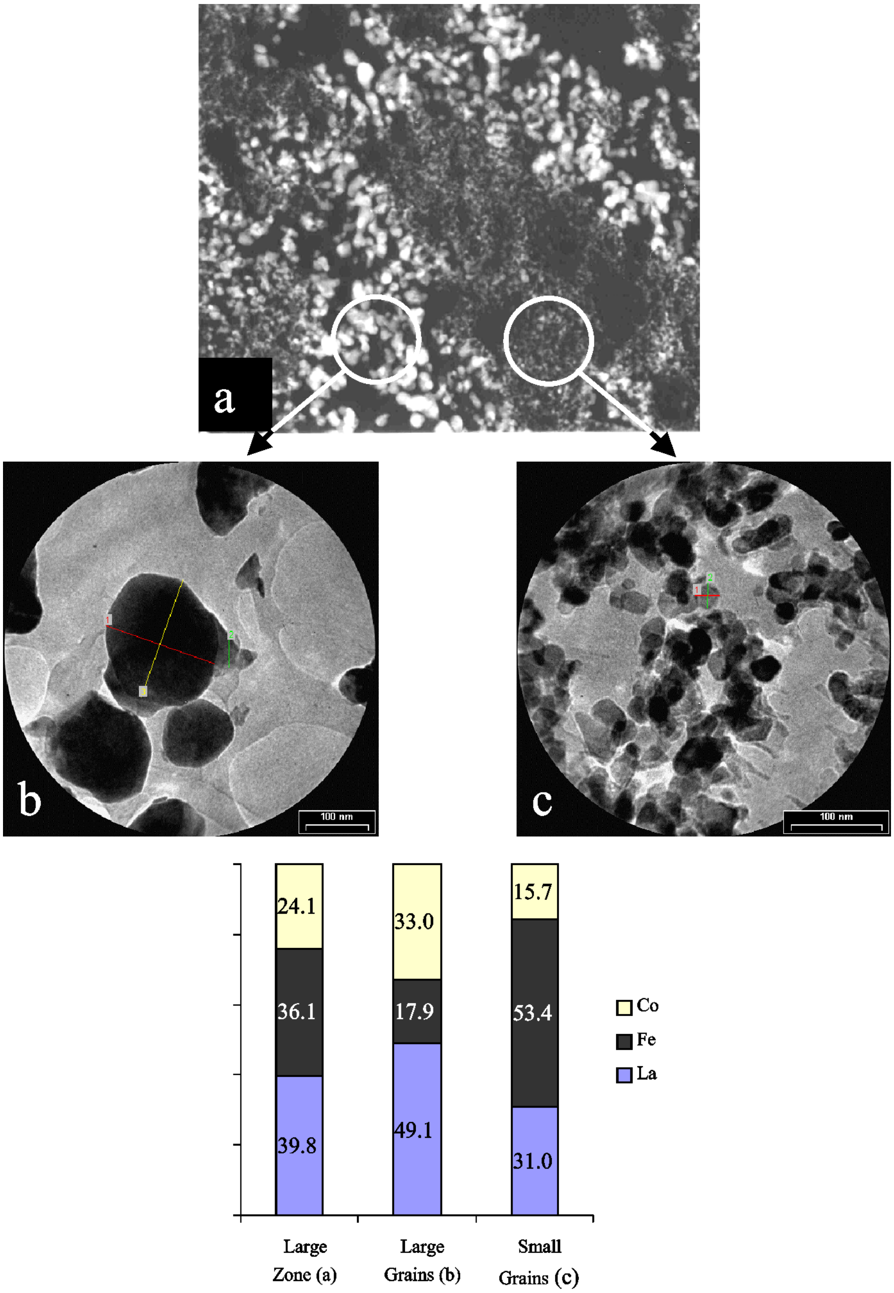

Fig. 4. TEM pictures of cut of $La_{0.7}Co_{0.4}Fe_{0.6}O_{3-\delta}$ (750 °C): (a) general view (×3000); (b) zone of large grains (×20,000); (c) of zone of small grains (×29,000). Average molar distribution (%) of cations in the whole sample (a), the large grains (b) and the small grains (c).

served by TEM is shown in Fig. 4. The existence of two types of grains is clearly shoen on low magnification (Fig. 4a). Zones of small grains (20–50 nm; Fig. 4c) surround zones of larger grains (120–190 nm; Fig. 4b). Analyzed by EDX, the elemental composition over a large area covering both the small- and large-grain regions is in agreement with that determined by ICP. If separately analyzed, small-grain regions exhibit a higher Fe content (53.4 mol%) than the large grain regions (17.9 mol%). Because the small grains are not pure γ-Fe_2O_3 particles and have too large a diameter to not be detected by XRD, Scheme 1C must be discarded. The different perovskite compositions in the small and large grains ($LaCo_{0.50}Fe_{0.50}O_3 + 0.61Fe_2O_3$ and $LaCo_{0.67}Fe_{0.33}O_3 + 0.015Fe_2O_3$, respectively) explains the nonsymmetric shape of the reflections observed on the XRD patterns and is consistent with the composition distribution taking the Mössbauer spectra into account.

The La content from one edge to the other of both small and large grains was studied by analyzing consecutive 8-nm-wide areas by EDX; results are plotted in Fig. 5. Whatever the size of the grain, 190 or 26 nm, the La content remained almost constant all along the grain. According to the unique central γ-Fe_2O_3 core hypothesis, the La content should decrease when analyzing the core; thus, this hypothesis also must be discarded. The only structure that can describe our compounds is that in Scheme 1B. Materials are then made of nanocores dispersed in a La–Co–Fe perovskite matrix.

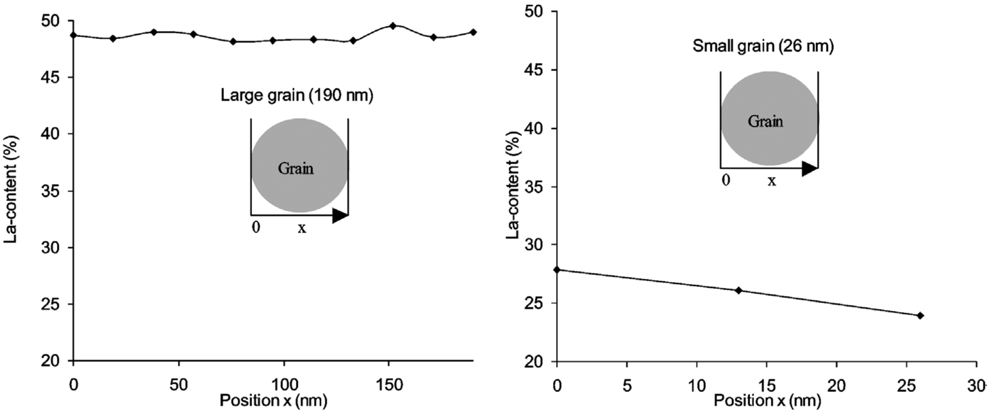

Fig. 5. Distribution of the La-content along the $La_{0.7}Co_{0.4}Fe_{0.6}O_{3-\delta}$ (750 °C) grains.

Because of the rejection of the excess B-cations via Fe into the γ-Fe_2O_3 phase, the perovskite phase average composition is Co-rich, up to $LaCo_{0.73}Fe_{0.27}O_3$ for $y = 0.2$. In a previous study [12] we showed that when the La–Co–Fe perovskites contain at least as much Co as Fe, they crystallize in the rhombohedral system. The observed cubic symmetry of the perovskite phase is probably caused by an epitaxial growth on the cubic γ-Fe_2O_3 cores. This interpretation could also explain the higher Fe content in the smaller grains than in the larger grains seen on TEM.

3.2. Reducibility and reduced catalysts

3.2.1. TPR

Because the metal phase is the active phase in Fischer–Tropsch synthesis, attention was given to reducibility. The reduction was first followed by TPR. The hydrogen consumption profiles are presented in Fig. 6 for the series of perovskites calcined at 750 and 900 °C.

The two series of catalysts present two zones of reduction, the maxima of which appear around 450 and 900 °C for calcination at 750 °C and a little higher for calcination at 900 °C. The lanthanum deficiency does not strongly influence the reduction temperature, but it does affect hydrogen consumption in the first zone of reduction; the volume of hydrogen consumed at low temperature increases linearly with y.

The other effect of the higher calcination temperature is to increase the separation between the two reduction zones. Whereas for the series at 750 °C, separation involves only a short return to the base line around 500 °C, the stability without any hydrogen consumption lasts between 50 °C for $y = 0$ and 120 °C for $0.1 \leqslant y \leqslant 0.4$ for the series at 900 °C. Consequently, all of the partially reduced perovskites are stable under reducing conditions around 500 °C. This stability of partially reduced oxides would allow their use as stable catalysts for Fischer–Tropsch synthesis.

The volumes of hydrogen needed for the reduction of 50 mg of fresh oxide at the two calcination temperatures are reported in Table 4. The amount of hydrogen consumed in the first zone (volumes V_1) increases with the lanthanum deficiency y: from 1.02 to 4.79 mL for the series at 750 °C, and from 0.90 to 4.85 mL for the series at 900 °C. Hydrogen consumption is practically independent on calcination temperature. The amounts of hydrogen consumed in the second zone (volumes V_2) do not vary much with varying y. The slight variations are due to the difficulty in achieving total reduction at 900 °C.

The perovskite phases of the samples $y = 0.2$ and $y = 0.4$ are noticeably identical (see Table 4). However, V_1 is largely higher for $y = 0.4$ (4.79 mL) than for $y = 0.2$ (3.22 mL). These two catalysts differ only in terms of their iron oxide content (0.26 Fe_2O_3 per perovskite for $y = 0.2$ and 0.38 for $y = 0.4$). A part of the hydrogen consumed in the first reduction zone can then be attributed to the reduction of γ-Fe_2O_3. The same conclusion can be drawn when comparing $y = 0$ and 0.1.

A partial reduction of the materials is then possible for the two series of perovskites. In a previous work [12] we showed that the partial reduction at 450 °C of $LaCo_{0.4}Fe_{0.6}O_3$ generates Co^0 particles on partially reduced perovskite. Here the presence of an additional phase of γ-Fe_2O_3, which seems to be reducible, would modify the nature of the metal phase generated by partial reduction, as can be seen by XRD, magnetic measurements and Mössbauer.

3.2.2. XRD

The diffractograms of the partially reduced oxides (1.5 h at 450 °C under 10% H_2/He) are presented in Fig. 7 for the two series. The crystalline structure of the perovskite phases was preserved whatever the calcination temperature and the lanthanum deficiency. The peak of γ-Fe_2O_3 detected on fresh samples for $y = 0.4$ disappeared to the benefit of a new peak around $2\theta = 53°$, attributed to a bcc Co–Fe alloy [30]. The lattice parameters of the two phases of the partially reduces samples are given in Table 5. The cubic lattice parameter of the perovskite phase does not vary much with y; from 3.908(3) to 3.920(3) Å for the series at 750 °C, and from 3.899(3) to 3.924(2) Å for the series at 900 °C. The cubic lattice parameter of the metal phase lies between 2.856(7) and 2.849(7) Å for the two series, corresponding to alloy composition between $(Co_{0.50}Fe_{0.50})^0$ and $(Co_{0.60}Fe_{0.40})^0$ [31]. The alloy crystallite medium size was estimated by the Debye–Scherrer formula as 10 nm for the series at 750 °C and 28 nm for the series at 900 °C.

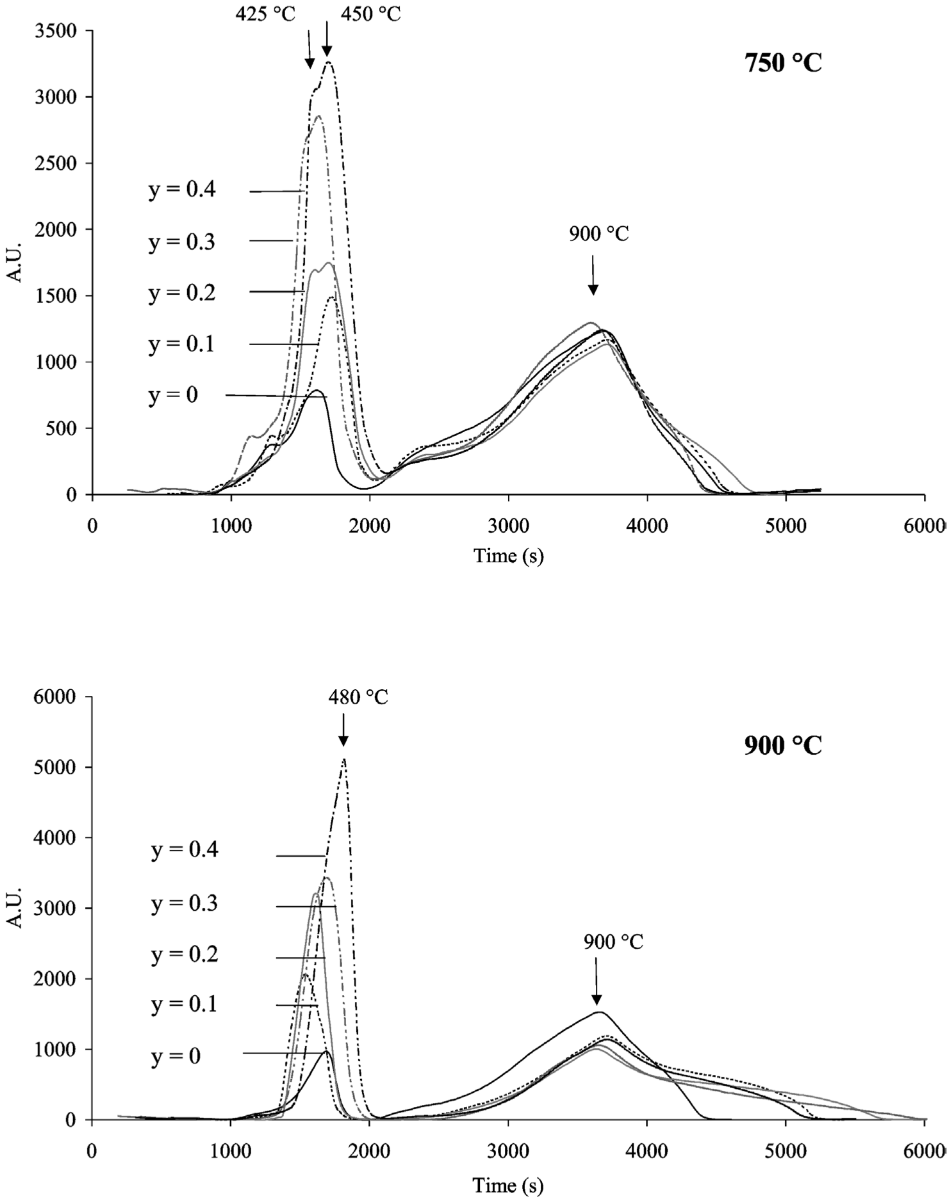

Fig. 6. TPR profiles of $La_{(1-y)}Co_{0.4}Fe_{0.6}O_{3-\delta}$. Calcined at 750 and 900 °C.

Table 4
Volume of hydrogen consumed during the two zones of reduction. V_1, first reduction around 450 °C; V_2, second reduction around 900 °C

y	Formula	750 °C		900 °C	
		V_1 (mL)	V_2 (mL)	V_1 (mL)	V_2 (mL)
0	$LaCo_{0,40}Fe_{0,60}O_3$	1.02	6.17	0.90	6.16
0.1	$LaCo_{0.46}Fe_{0.54}O_3 + 0.11Fe_2O_3$	2.21	6.07	2.16	6.14
0.2	$LaCo_{0.73}Fe_{0.27}O_3 + 0.26Fe_2O_3$	3.22	5.93	3.01	5.58
0.3	$LaCo_{0.61}Fe_{0.39}O_3 + 0.26Fe_2O_3$	3.83	6.01	3.75	5.36
0.4	$LaCo_{0.70}Fe_{0.30}O_3 + 0.38Fe_2O_3$	4.79	5.31	4.85	5.46

3.2.3. *Magnetic measurements*

In view of quantifying the metal generated by partial reduction, magnetization cycles were performed on partially reduced samples. The cycles for the two series of partially reduced catalysts are shown in Fig. 8, and the corresponding saturation magnetizations are given in Table 5. Saturation magnetization increased with the lanthanum deficiency, from 3.3 to 25.3 emu g^{-1} for the series at 750 °C and from 1.3 to 33.4 emu g^{-1} for the series at 900 °C. Saturation magnetizations at ambient temperature for various iron-based alloys depending on their composition have been given previously [32]. The content in alloy (whose composition is determined from the lattice parameter) can then be deduced from the M_S values. For the two samples $y = 0.1$, the lattice parameter could not be determined by XRD, and so the alloy composition was taken to be equal to that of the sample $y = 0.2$ in the same series.

As reported previously, for stoichiometric perovskites ($y = 0$), the metal phase generated by reduction is only cobalt [12]. In contrast to the partially reduced stoichiometric perovskites, in which the amount of metal (Co^0) decreases with the initial calcination temperature (by 2.1% for $y = 0$ at 750 °C and 0.8% for $y = 0$ at 900 °C), the amount of metal formed after partial reduction of deficient perovskites increased with the initial cal-

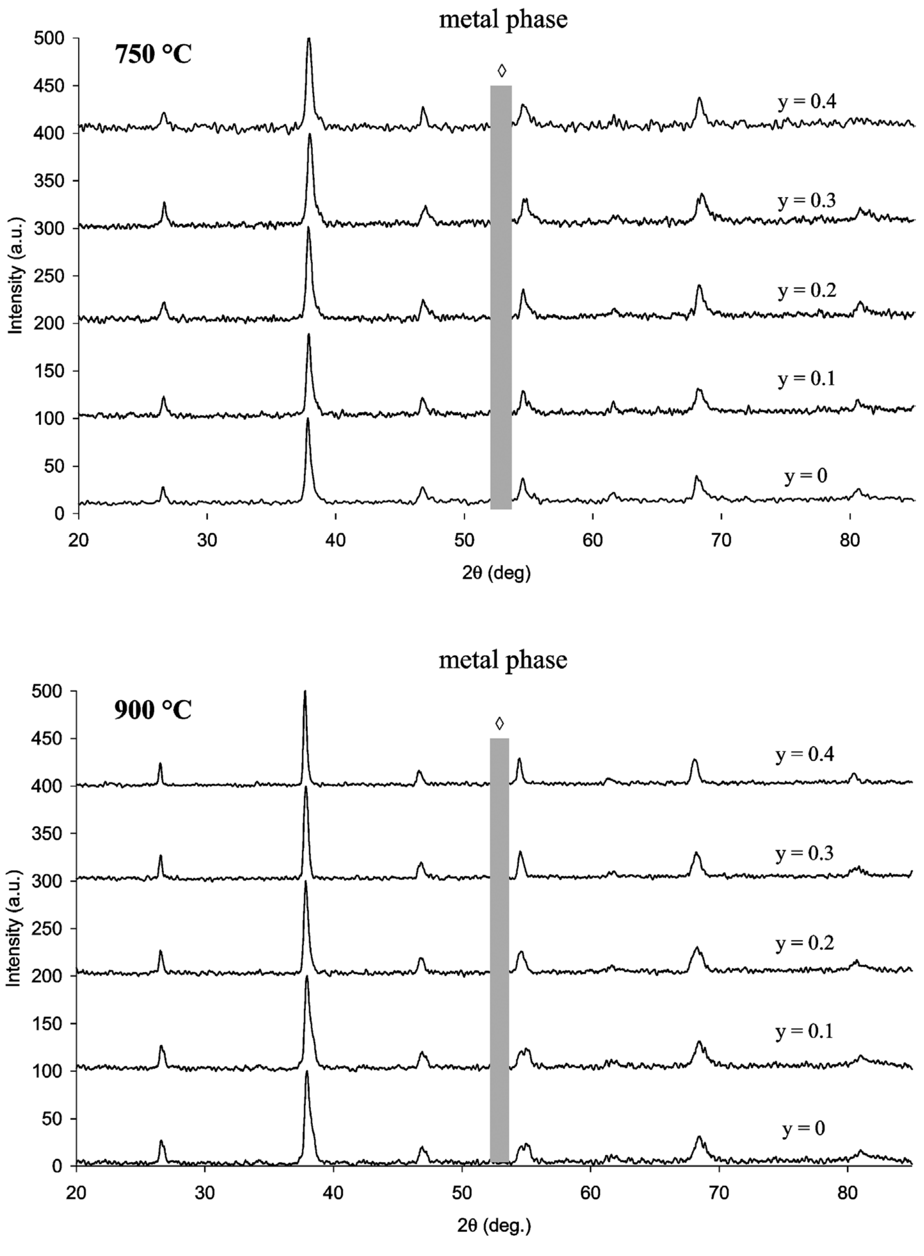

Fig. 7. Diffractograms of $La_{(1-y)}Co_{0.4}Fe_{0.6}O_{3-\delta}$. Calcined at 750 and 900 °C, after partial reduction at 450 °C.

Table 5

Lattice parameters of oxide and metal phases after partial reduction of the two $La_{(1-y)}Co_{0.4}Fe_{0.6}O_3$ series. Saturation magnetization (M_S) after partial reduction. Amount of metal (wt%) and formula of the metal phase

y	750 °C			900 °C		
	a(oxide) (Å)	a(metal) (Å) [composition]	M_S (emu g^{-1}) [metal amount]	a(oxide) (Å)	a(metal) (Å) [composition]	M_S (emu g^{-1}) [metal amount]
0	3.920(3)	– [Co]	3.3 [2.1 wt%]	3.899(3)	– [Co]	1.3 [0.8 wt%]
0.1	3.921(3)	– [$Co_{0.50}Fe_{0.50}$]	11.0 [4.8 wt%]	3.921(3)	–	9.5 [4.0 wt%]
0.2	3.914(3)	2.856(7) [$Co_{0.50}Fe_{0.50}$]	15.2 [6.6 wt%]	3.919(3)	2.853(7) [$Co_{0.55}Fe_{0.45}$]	15.9 [6.8 wt%]
0.3	3.908(3)	2.856(7) [$Co_{0.50}Fe_{0.50}$]	21.8 [9.5 wt%]	3.911(3)	2.854(7) [$Co_{0.53}Fe_{0.47}$]	23.4 [10.1 wt%]
0.4	3.914(3)	2.854(7) [$Co_{0.53}Fe_{0.47}$]	25.3 [10.9 wt%]	3.924(2)	2.849(7) [$Co_{0.60}Fe_{0.40}$]	33.4 [14.1 wt%]

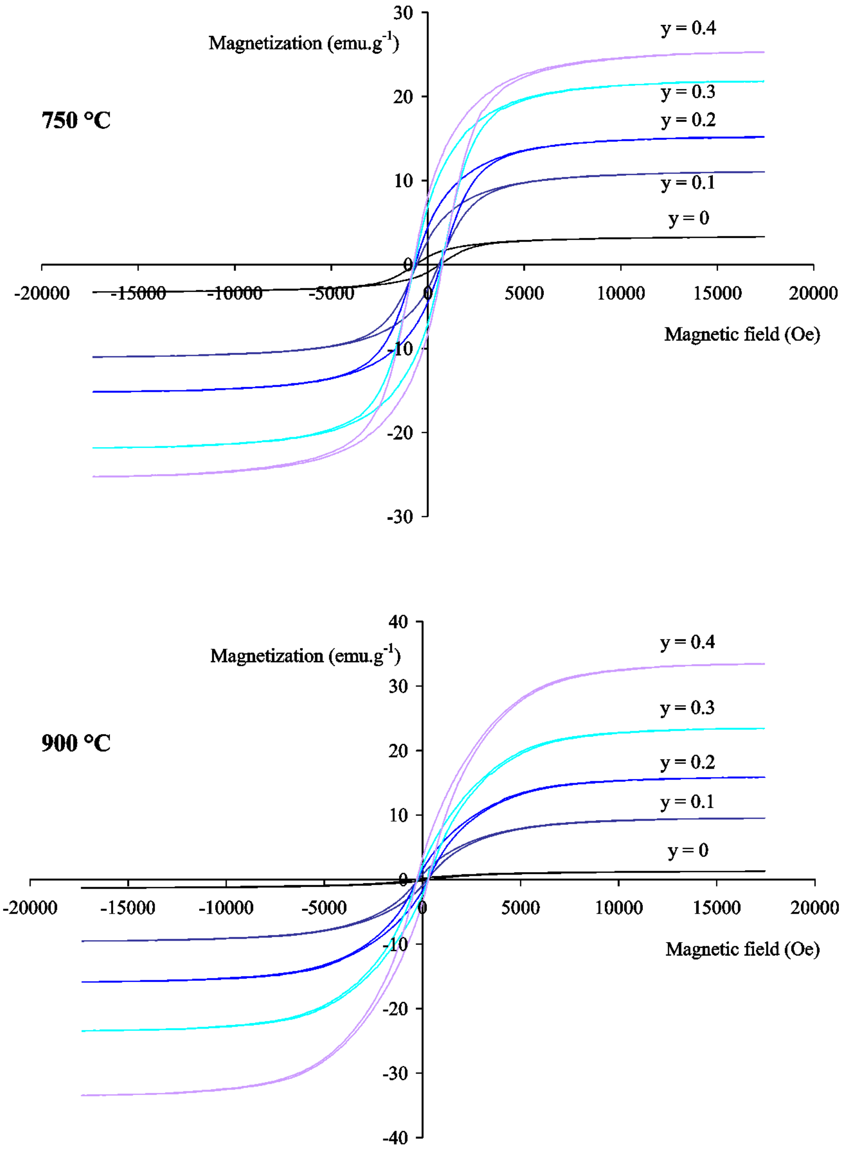

Fig. 8. Magnetization cycles of $La_{(1-y)}Co_{0.4}Fe_{0.6}O_{3-\delta}$. Calcined at 750 and 900 °C, after partial reduction at 450 °C.

cination temperature (10.9% for $y = 0.4$ at 750 °C, compared with 14.1% at 900 °C).

The amount of metal generated by partial reduction increased significantly with increasing lanthanum deficiency. The maximum was obtained for the sample $y = 0.4$ calcined at 900 °C.

Note that for the series at 750 °C, the saturation magnetization of reduced samples was difficult to reach (see Fig. 8), accounting for a superparamagnetic behavior, in accordance with the small particle size calculated from XRD (10 nm). This was not the case for the series at 900 °C.

3.2.4. Mössbauer experiments

To understand the origin of the Co–Fe alloy, Mössbauer experiments were carried out on partially reduced deficient perovskites. The Mössbauer spectrum of $y = 0.3$ (calcination at 750 °C) after partial reduction is shown in Fig. 9. The experimental spectrum is the sum of two sextets, the characteristics of which are given in Table 6. The isomeric shift of the first sextet ($\delta = 0.345\ \mathrm{mm\,s^{-1}}$) and the value of the hyperfine field ($H = 537$ kG) allowed its attribution to Fe^{3+} in the B sites of the perovskite phase. The sextet of Fe^{3+} in γ-Fe_2O_3 encountered in the fresh oxide (see Table 2) disappeared to the benefit of another sextet, whose isomeric shift close to 0 ($\delta = -0.003\ \mathrm{mm\,s^{-1}}$) is characteristic of metal iron. The value of the hyperfine field ($H = 339$ kG) is in accordance with an alloy phase of composition $Fe_{0.5}Co_{0.5}$ (342 kG) [33]. Partial reduction of the perovskite involved the total reduction of the γ-Fe_2O_3 cores into metal iron, which combined with the metal cobalt coming from perovskite reduction to form a $Co_{0.5}Fe_{0.5}$ alloy.

Combining the various characterization results allowed us to determine the formulae of the partially reduced perovskites. These are presented in Table 7.

The amount of metal generated by partial reduction increased with increasing La deficiency y and with increasing

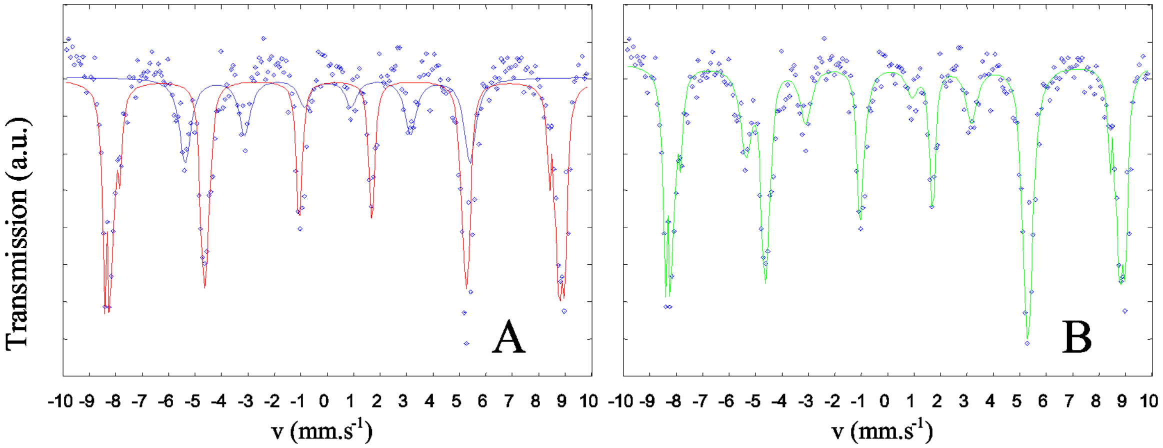

Fig. 9. Partially reduced $La_{0.7}Co_{0.4}Fe_{0.6}O_{3-\delta}$ experimental Mössbauer spectrum at 4 K and its deconvoluted components (A) or their sum (B).

Table 6
Characteristics of the $La_{0.7}Co_{0.4}Fe_{0.6}O_{3-\delta}$ (after partial reduction) deconvoluted Mössbauer components

Component	δ (mm s^{-1})	Δ (mm s^{-1})	H (kG)	Attribution	(%)
Sextet	0.345	0	537	Fe^{3+} (B-site)	74
Sextet	−0.003	0	339	Fe^0	26

initial calcination temperature of the oxide, except for $y = 0$ and $y = 0.1$. For the system $y = 0.2$, the γ-Fe_2O_3 phase was difficult to reduce, possibly because of its higher Co content compared with other systems. The proportion of iron in the perovskite was increased after reduction.

3.2.5. *TEM*

The cut of 750 °C calcined $La_{0.7}Co_{0.4}Fe_{0.6}O_{3-\delta}$ material after partial reduction observed by TEM is shown in Fig. 10. As in the fresh catalyst, the grains are heterogeneous in size and composition. Mean grain size was the same in the reduced sample and the fresh sample, for both large (100–200 nm) and small (20–50 nm) grains. The morphology was not modified by reduction. EDX analysis found no grains free of lanthanum and no isolated particles of alloy. Fig. 10 shows the mean molar composition in cations in the whole sample, as well as in the small and large grains. The grain composition of the reduced sample was similar to that determined before reduction, small grains are enriched in iron compared with large grains. The lanthanum content profile along the grains (Fig. 10) reveals that it was always higher in the center of the grain than at the edge. The metallic phase detected by XRD, magnetic measurements, and Mössbauer would then be located at the surface of the catalyst grains.

3.3. *Catalytic results*

Before testing the reactivity of the partially reduced systems in Fischer–Tropsch synthesis, we evaluated their ability to initiate the reaction by studying the CO dissociation reaction under atmospheric pressure. The CO dissociation in to $C_{surface}$ and $O_{surface}$ is considered the limiting step of the Fischer–Tropsch reaction [34].

3.3.1. *CO dissociation*

CO conversion into CO_2 and $C_{surface}$ for the partially reduced series of perovskites calcined at 750 and 900 °C is shown in Fig. 11. Among the catalysts of a single series, the activity in CO dissociation increased with increasing lanthanum deficiency, due to the increased metal generated by reduction. For the series at 750 °C, CO conversion increased almost linearly from 12% for $y = 0$ (2.1 wt% of metal) to 19% for $y = 0.4$ (10.9 wt% of metal).

Comparing the two series, it appears that despite their higher metal content, the catalysts of the series at 900 °C had weaker activity in CO conversion than those of the series at 750 °C. For example, for $y = 0.4$ (14.1 wt% of metal), CO conversion was only 12%. In these systems, the larger metallic particle size (28 nm compared to 10 nm for the series at 750 °C) led to a decrease in surface/volume ratio, and the higher metal content did not have a beneficial effect on catalytic activity.

Table 7
Developed formulation of partially reduced $La_{(1-y)}Co_{0.4}Fe_{0.6}O_{3-\delta}$ oxides calcined at 750 and 900 °C

y	Calcination at 750 °C and partial reduction	Calcination at 900 °C and partial reduction
0	$Co^0_{0.085}/LaCo^{2+}_{0.19}Co^{3+}_{0.13}Fe_{0.60}O_{2.78}$	$Co^0_{0.03}/LaCo^{2+}_{0.31}Co^{3+}_{0.06}Fe_{0.60}O_{2.80}$
0.1	$(Co_{0.50}Fe_{0.50})^0_{0.22}/LaCo^{2+}_{0.35}Fe_{0.65}O_{2.82}$	$(Co_{0.55}Fe_{0.45})^0_{0.18}/LaCo^{2+}_{0.36}Fe_{0.64}O_{2.82} + 0.02\ FeO_x$
0.2	$(Co_{0.50}Fe_{0.50})^0_{0.33}/LaCo^{2+}_{0.56}Fe_{0.44}O_{2.72} + 0.09FeO_x$	$(Co_{0.55}Fe_{0.45})^0_{0.34}/LaCo^{2+}_{0.54}Fe_{0.46}O_{2.73} + 0.09FeO_x$
0.3	$(Co_{0.50}Fe_{0.50})^0_{0.47}/LaCo^{2+}_{0.37}Fe_{0.63}O_{2.82} + 0.02FeO_x$	$(Co_{0.53}Fe_{0.47})^0_{0.50}/LaCo^{2+}_{0.34}Fe_{0.66}O_{2.83} + 0.01FeO_x$
0.4	$(Co_{0.50}Fe_{0.50})^0_{0.58}/LaCo^{2+}_{0.39}Fe_{0.61}O_{2.80} + 0.09FeO_x$	$(Co_{0.60}Fe_{0.40})^0_{0.75}/LaCo^{2+}_{0.25}Fe_{0.75}O_{2.84}$

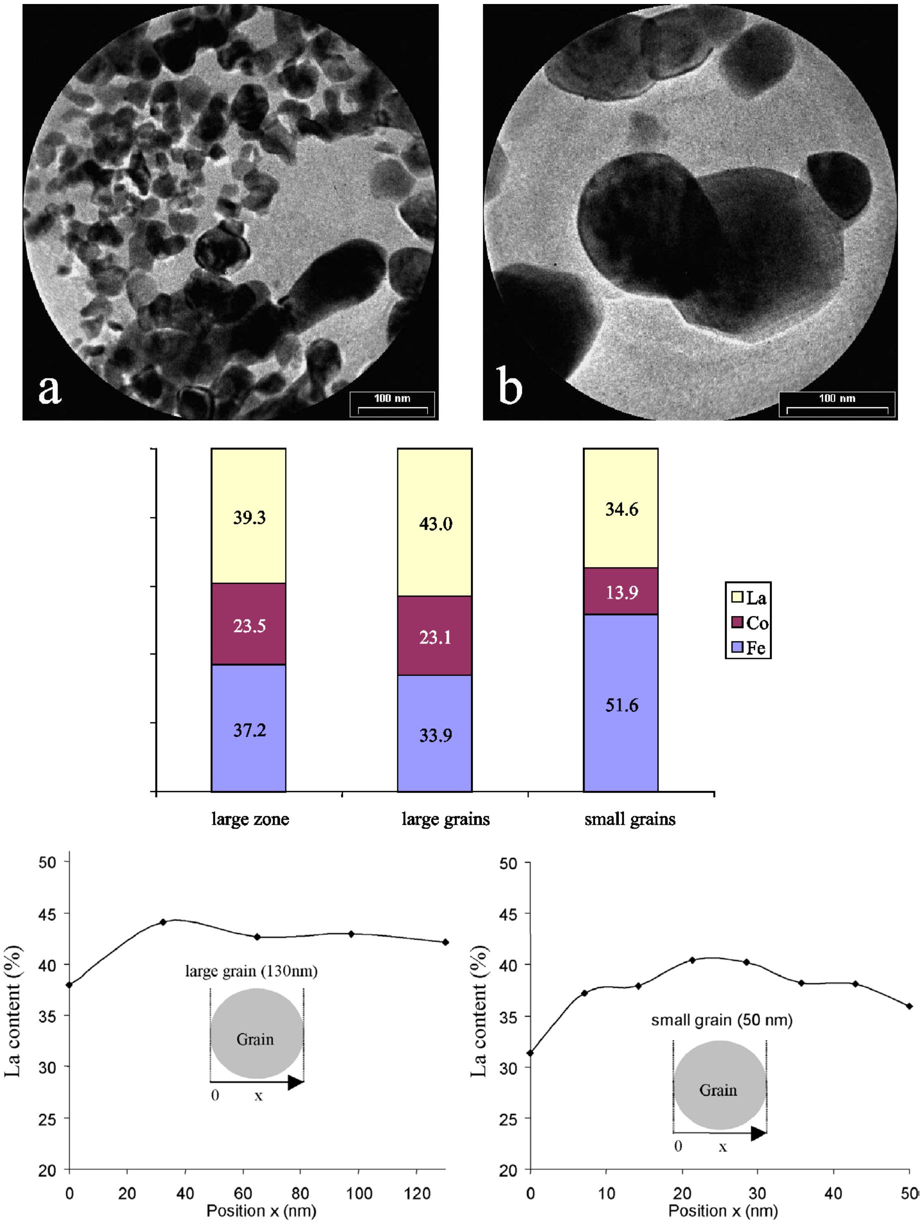

Fig. 10. TEM pictures of cut of $La_{0.7}Co_{0.4}Fe_{0.6}O_{3-\delta}$ (750 °C) after partial reduction (top). Average molar distribution (%) of cations in the sample (middle). Distribution of the La-content along the grains (bottom).

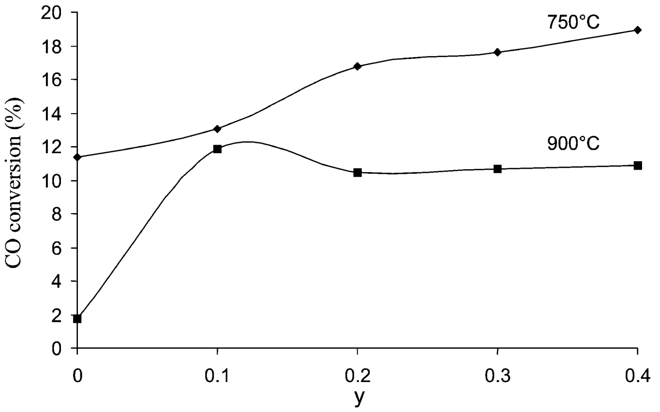

Fig. 11. CO conversion (%) versus lanthanum deficiency y for the two series of catalysts (calcined at 750 and 900 °C), reaction of CO dissociation.

3.3.2. *Fischer–Tropsch synthesis*

After the initial evaluation of the catalytic activity by CO dissociation at atmospheric pressure, the catalysts were tested in real Fischer–Tropsch synthesis conditions under 1 MPa pressure (see Section 2). The CO conversion obtained for partially reduced catalysts of the series at 750 °C, as well as the most active catalyst of the second series ($y = 0.4$ at 900 °C), are shown in Fig. 12. The increased CO conversion with y is in accordance with the results obtained by CO dissociation. A temperature of 230 °C was sufficient to obtain a CO conversion of 4.5% with the catalyst $La_{0.6}Co_{0.4}Fe_{0.6}O_{3-\delta}$ ($y = 0.4$), whereas the system in which $y = 0$ required an increase in reaction temperature to 280 °C to reach a conversion of the same order (3.7%). At the same La deficiency ($y = 0.4$), as foreseen by CO dissociation,

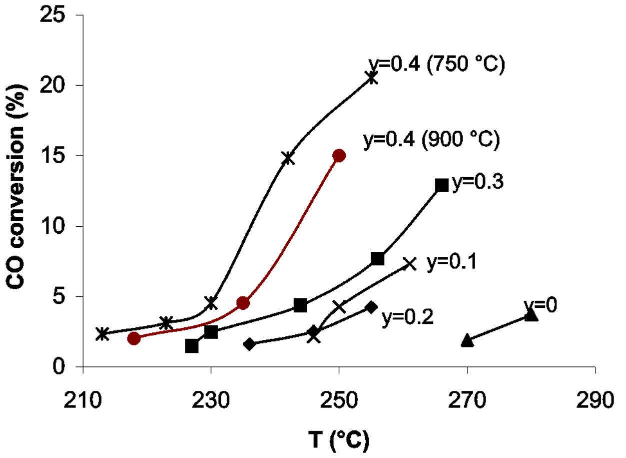

Fig. 12. CO conversion (%) vs. Fischer–Tropsch reaction temperature for the catalysts of the series at 750 °C and $y = 0.4$ at 900 °C.

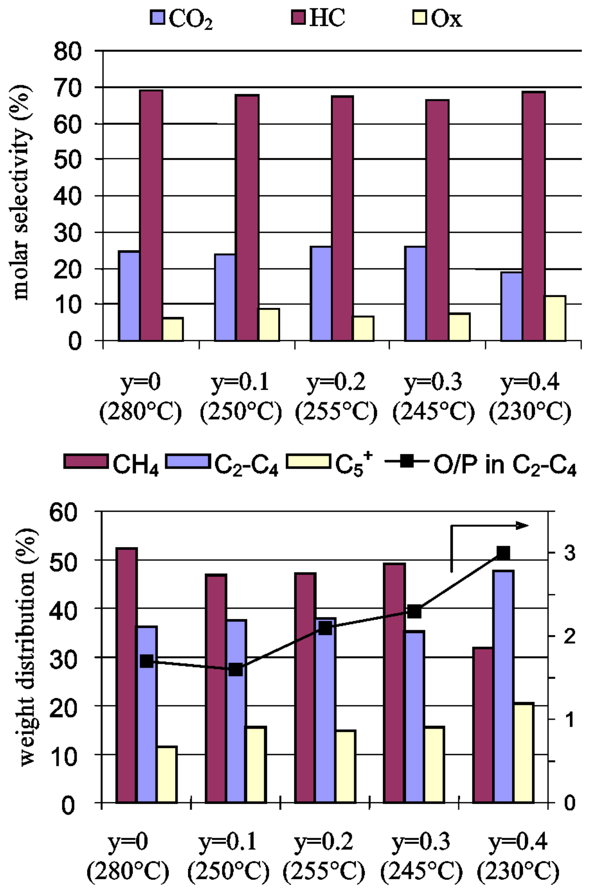

Fig. 13. Fischer–Tropsch product distribution at CO isoconversion of 5% for the catalysts of the series at 750 °C.

the activity of the catalyst calcined at 900 °C was lower than that of the catalyst calcined at 750 °C.

The product distribution obtained at CO isoconversion of almost 5% is shown in Fig. 13. At isoconversion, the product distribution did not vary much among the series. Molar selectivity to CO_2 varied between 26% for $y = 0.2$ and $y = 0.3$ and 19% for $y = 0.4$. Hydrocarbon fraction was always the major part of the products (around 67–69% of molar selectivity). The molar selectivity into oxygenated products (mainly methanol and ethanol) ranged from 6.4% for $y = 0$ and 12.1% for $y = 0.4$. More than a catalyst effect, the formation of such oxygenated products seems to be favored by lower reaction temperatures.

In comparison with the literature data on FeCo alloys in Fischer–Tropsch, our catalytic systems appeared to produce little CO_2. Previous studies of Co–Fe alloys deposited on zeolites at a 3% conversion of CO found variable molar selectivity to CO_2 depending on the support, 41% with HZMS-5 and 51% with HY zeolite [35], whereas at the same order of conversion, the CO_2 selectivity of our systems was only around 20%.

In the hydrocarbon fraction, the ratio $[C_2–C_4]/C_5^+$ was independent of y and equals 2.4 (weight distribution). For lanthanum deficiency up to $y = 0.3$, methane was the main hydrocarbon fraction (accounting for 47–52% of the total weight of the hydrocarbon fraction). For the most deficient catalyst ($y = 0.4$), decreasing the reaction temperature (to 230 °C) induced a significant decrease in methane formation, to only 32% of the total weight. For this catalyst, at CO conversion of 5%, the main fraction was the $C_2–C_4$ fraction (48% of the total weight). The decrease in reaction temperature changed the olefin proportion in the $C_2–C_4$ fraction. Olefins were clearly favored for $y = 0.4$ (230 °C), because the olefin/paraffin ratio reached the value of 3 (75% of olefins in this fraction). This is in accordance with a decrease in the secondary reactions of olefin readsorption and their consecutive hydrogenation at low reaction temperature [36,37].

The selectivity into olefins in the light fraction is much higher than that reported by Chen et al. [38] and Ishihara et al. [39] on $FeCo_3$-based catalysts. Chen et al. reported [37] an olefin/paraffin ratio of 0.2–0.5 (depending on the reducing procedure) over $FeCo_3$/carbon catalyst, whereas Ishihara et al. [38] reported olefin/paraffin ratios in the $C_2–C_5$ fraction of 1.5 over TiO_2 and 0.6 over SiO_2. The FeCo-based catalysts studied by Butt et al. [35] were also poorly selective into light olefins (olefin/paraffin ratios in the $C_2–C_3$ fraction between 0.3 and 0.7).

To summarize this comparative study of the catalysts, it appears that the amount of metal phase generated by controlled reduction did not significantly affect the selectivity of the reaction but did direct Fischer–Tropsch activity. $La_{0.6}Co_{0.4}Fe_{0.6}O_{3-\delta}$ exhibited high CO conversion at moderate reaction temperatures (21% conversion at 255 °C), with such temperatures allowing high selectivity toward light olefins.

The aim of the present study—to increase the metal amount to improve the catalytic performance of the La–Co–Fe perovskites—thus was largely achieved. With the previous non-La-deficient perovskite [12] (which corresponds to $y = 0$ in the present work), Fischer–Tropsch activity was much lower (2% of CO conversion at 270 °C).

3.3.3. *Long-term activity*

The perovskite $La_{0.7}Co_{0.4}Fe_{0.6}O_{3-\delta}$ of the series at 750 °C corresponding to a La deficiency $y = 0.3$ was extensively characterized before catalytic tests and after reducing treatments. Long-term Fischer–Tropsch activity studies were then performed on that catalyst, under the same experimental condi-

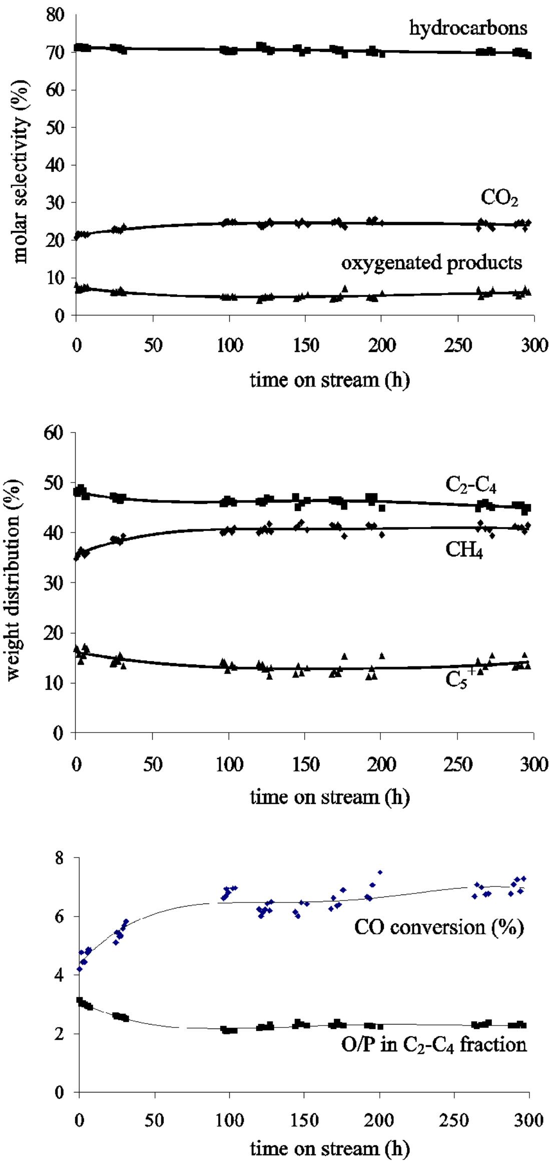

Fig. 14. Fischer–Tropsch product distribution, CO conversion and O/P fraction, vs. time on stream for $La_{0.7}Co_{0.4}Fe_{0.6}O_{3-\delta}$ (750 °C) at 250 °C.

tions as before, at 250 °C, for 300 h. The results, presented in Fig. 14, show that CO conversion increased in the first 75 h of catalytic testing from 4.5 to almost 7%, and then remained quite constant over the next 225 h. No deactivation was observed.

During the test, the product distribution remained almost unchanged. As seen for the CO conversion, an initial period of 75 h was necessary to reach the steady state. Hydrocarbons represented 70% (in mol) of the products; the molar selectivity into CO_2 and oxygenated products stabilized at around 25 and 5%, respectively. Among the hydrocarbons, the C_2–C_4 fraction represented 46% of the total weight, 41% for CH_4 and 13% for heavier hydrocarbons. The olefin/paraffin ratio in the C_2–C_4 fraction decreased initially from 3 to 2.3, and remained constant at this value.

3.4. Characterization after testing

Fig. 15 presents diffractograms of the $La_{0.7}Co_{0.4}Fe_{0.6}O_{3-\delta}$ catalyst after partial reduction at 450 °C and compares them with those obtained after CO dissociation reaction and after Fischer–Tropsch synthesis. As explained earlier, after partial reduction, the perovskite crystalline structure was preserved, and the reduction of cobalt cations in the perovskite along with the reduction of the γ-Fe_2O_3 cores gave rise to a $(Co–Fe)^0$ alloy detected by XRD. After CO dissociation, the perovskite structure was still preserved, and the alloy was still detectable by XRD. However, after Fischer–Tropsch synthesis, although the perovskite phase was not modified, the alloy main diffraction peak disappeared. No carbide phase was detected, neither χ-Fe_5C_2 (thought to be the active phase by many authors [40–44]) nor cobalt carbide Co_2C, unstable at ambient temperature but detected on bimetallic Co–Fe Fischer–Tropsch catalysts after testing [45,46]. One explanation for this finding could be the redispersion of metal aggregates into smaller particles (metal and/or carbide) that are not detectable by XRD. This assumption could not have been confirmed by TEM observation of the catalyst after Fischer–Tropsch reaction, because no isolated particles of Co–Fe (without lanthanum) were detected by TEM.

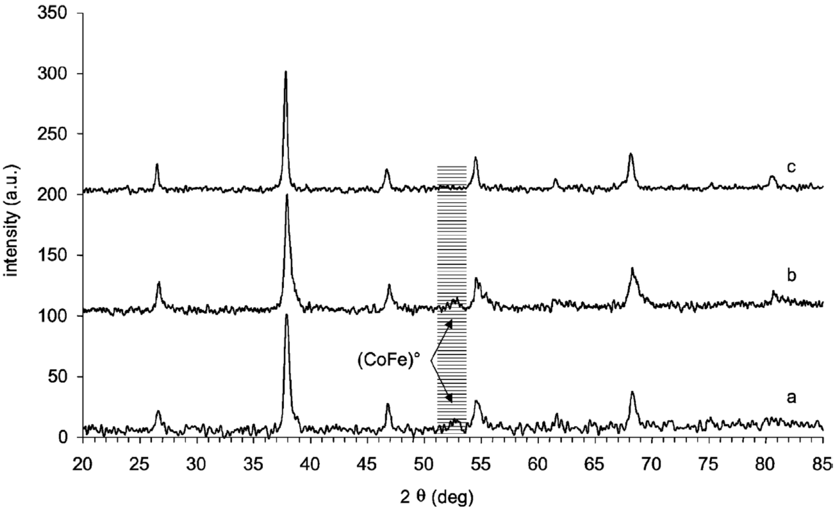

Fig. 15. Diffractograms of $La_{0.7}Co_{0.4}Fe_{0.6}O_{3-\delta}$ (750 °C): (a) after partial reduction, (b) after CO dissociation, (c) after SFT.

4. Conclusions

$La_{(1-y)}Co_{0.4}Fe_{0.6}O_{3-\delta}$ materials prepared by the thermal decomposition of mixed La–Co–Fe propionates did not lead to La-deficient perovskites, although single perovskite phases were observed by XRD up to a La deficiency of 0.3. Mössbauer spectroscopy revealed the presence of an Fe_2O_3 phase in addition to the perovskite. Magnetic measurements were in favor of the iron oxide phase γ-Fe_2O_3 instead of α-Fe_2O_3. According to both micrographs and EDX analysis, iron oxide particles were too small to diffract X-rays. They were surrounded by a non-cation-deficient perovskite phase. $La_{(1-y)}Co_{0.4}Fe_{0.6}O_{3-\delta}$ materials thus may be considered nano-composites. The very small size of some γ-Fe_2O_3 particles made the saturation of their magnetization difficult to reach. However, these composites already exhibited very strong coercive fields (around 8500 Oe at 4 K). Even when Co-rich (e.g., $LaCo_{0.73}Fe_{0.27}O_3$ for $y = 0.2$), the perovskite-type phase crystallized in the cubic system. This unexpected feature of $LaCo_xFe_{(1-x)}O_3$ perovskite series being either orthorhombic for $x < 0.5$ or rhombohedral for $x \geqslant 0.5$ can be explained by an epitaxial growth of the perovskite phase over nanosize cubic γ-Fe_2O_3 cores.

The study of the reducibility of these composite oxides showed that the γ-Fe_2O_3 nanocores were reducible at 450 °C under hydrogen. This partial reduction gives rise to a metal phase, the composition of which depends on the initial calcination temperature of the material (i.e., $Co_{0.5}Fe_{0.5}$ for the series at 750 °C and $Co_{0.6}Fe_{0.4}$ for $y = 0.4$ at 900 °C). The cobalt cations extracted from the cubic perovskite by reduction are replaced by iron cations of the Fe_2O_3 phase, and the oxide structure then is not destroyed by reduction. The amount of metal alloy was directly related to the initial lanthanum deficiency (i.e., increases with increasing y) and increased with increasing initial calcination temperature of the oxides (10.9 wt% for $y = 0.4$ at 750 °C and 14.1 wt% for $y = 0.4$ at 900 °C). The increase in calcination temperature came with an increase in metal particle size (10 nm for $y = 0.4$ at 750 °C and 28 nm for $y = 0.4$ at 900 °C).

Fischer–Tropsch activity is directly related to the amount of metal alloy generated by partial reduction. Thus, the activity increases with increasing lanthanum deficiency, that is, with an increasing amount of γ-Fe_2O_3 nanocores in the fresh oxide. For a similar lanthanum deficiency, the increasing amount of metal with increasing initial calcination temperature has no beneficial effect on catalytic activity, because of the concomitant enlargement of the alloy particle size.

The most deficient catalyst ($y = 0.4$) exhibited excellent C_2–C_4 olefin selectivity. The decreased reaction temperature with an increasing amount of metal led to diminished secondary reactions of olefin readsorption and their consecutive hydrogenation. The catalysts exhibited high stability under testing for 300 h.

The aim of improving catalytic activity by increasing the amount of metal extractable by reduction with lanthanum deficiency, without generating any real A-site deficiency, was achieved. This is because the activity of the best catalyst of this series ($y = 0.4$, CO conversion of 21% at 255 °C) was much higher than that of the best catalyst of the previous series ($y = 0$ in the present work, CO conversion of 2% at 270 °C).

References

[1] L.J. Tejuca, J.L.G. Fierro, Properties and Applications of Perovskite Type Oxides, Dekker, New York, 1993.
[2] M.A. Peña, J.L.G. Fierro, Chem. Rev. 101 (2001) 1981.
[3] S. Lee, K.S. Lee, S.K. Woo, J.W. Kim, T. Ishihara, D.K. Kim, Solid State Ionics 158 (3–4) (2003) 287.
[4] B.T. Cong, P.N. Anh Huy, N.H. Long, J. Magn. Magn. Mater. 262 (3) (2003) 437.
[5] H. Arai, T. Yamada, K. Eguchi, T. Seiyama, Appl. Catal. 26 (1986) 265.
[6] T. Nitadori, M. Misono, J. Catal. 93 (1985) 93.
[7] K.S. Chan, J. Ma, S. Jaenicke, G.K. Chuah, Appl. Catal. A 107 (1994) 337.
[8] R. Doshi, C.B. Alcock, J.J. Carberry, Catal. Lett. 18 (1993).
[9] C. Petit, A. Kiennemann, P. Chaumette, O. Clause, French Patent 92/11638 (1992).
[10] J.O. Pentuchi, M.A. Ulla, J.A. Marcos, E.A. Lombardo, J. Catal. 70 (1981) 1787.
[11] L. Wachowski, S. Zielinski, A. Burewicz, Acta Chim. Sci. Hung. 106 (1981) 217.
[12] L. Bedel, A.C. Roger, C. Estournès, A. Kiennemann, Catal. Today 85 (2003) 207.
[13] J.W. Stevenson, T.R. Armstrong, L.R. Pederson, J. Li, C.A. Lewinshon, S. Baskaran, Solid State Ionics 113–115 (1998) 571.
[14] D. Waller, J.A. Lane, J.A. Kilner, B.C.H. Steele, Solid State Ionics 86–88 (1996) 767.
[15] F.W. Poulsen, Solid State Ionics 129 (2000) 145.
[16] G.Ch. Kostogloudis, Ch. Ftikos, Solid State Ionics 126 (1999) 143.
[17] V.V. Kharton, A.P. Viskup, E.N. Naumovich, A.A. Tonoyan, O.P. Reut, Mater. Res. Bull. 33 (7) (1998) 1087.
[18] A.R. Chakhmouradian, R.H. Mitchell, P.C. Burns, J. Alloys Compd. 307 (2000) 149.
[19] A.C. Roger, C. Petit, A. Kiennemann, J. Catal. 167 (1997) 447.
[20] H. Provendier, C. Petit, J.L. Schmitt, A. Kiennemann, J. Mater. Sci. 34 (1999) 4121.
[21] M. Evain, U-Fit V 1.3 Institut des Matériaux de Nantes, 1992.
[22] G. Dezanneau, A. Sin, H. Roussel, M. Audier, H. Vincent, J. Solid State Chem. 173 (1) (2003) 216.
[23] P. Poix, Bull. Soc. Ceram. 72 (1966) 1.
[24] V.C. Belessi, T.V. Bakas, C.N. Costa, A.M. Efstathiou, P.J. Pomonis, Appl. Catal. B 28 (2000) 13.
[25] V.C. Belessi, P.N. Trikalitis, A.K. Lavados, T.V. Bakas, P.J. Pomonis, Appl. Catal. A 177 (1999) 53.
[26] J.G. Stevens, A.M. Khasanov, J.W. Miller, H. Pollak, Z. Li (Eds.), Mössbauer Mineral Handbook, Mössbauer Effect Data Center, 1998.
[27] J. Kaczér, T. Shalnikova, in: International Conference on Magnetism, Nottingham, 1964.
[28] O. Jarjayes, P.H. Fries, G. Bidan, J. Magn. Magn. Mater. 137 (1994) 205.
[29] L. Bedel, A.C. Roger, C. Estournès, A. Kiennemann, in: Proceedings of 9th International Symposium on Heterogeneous Catalysis, Varna, 2000, p. 519.
[30] Powder Diffraction File, International Center for Diffraction Data, File 48-1818.
[31] W.C. Ellis, E.S. Greiner, Trans. Am. Soc. Met. 29 (1941) 415.
[32] Landolt Börstein—New Series III/19a 189.
[33] Landolt Börstein—New Series III/19a 157.
[34] P. Chaumette, P. Courty, A. Kiennemann, B. Ernst, Top. Catal. 2 (1995) 117.
[35] J.B. Butt, T.-A. Lin, L.H. Schwartz, J. Catal. 97 (1986) 261.
[36] H. Schulz, M. Claeys, Appl. Catal. A 186 (1999) 109.
[37] J. Patzlaff, Y. Liu, C. Graffmann, J. Gaube, Appl. Catal. A 186 (1999) 145.
[38] A.A. Chen, M. Kaminsky, G.L. Geoffroy, M.A. Vannice, J. Phys. Chem. 90 (1986) 4810.

[39] T. Ishihara, K. Eguchi, H. Araï, Appl. Catal. A 30 (1987) 225.

[40] H. Storch, N.G. Golumbic, R.B. Anderson, The Fischer–Tropsch and Related Syntheses, Wiley, New York, 1951.

[41] C.D. Frohning, H. Kölbel, M. Ralch, W. Rottig, F. Schnur, H. Schulz, in: J. Falbe (Ed.), Chemierohstoffe aus Kohle, Georg Thieme Verlag, Stuttgart, 1977, p. 219.

[42] H. Schulz, G. Schaub, M. Claeys, T. Riedel, Appl. Catal. A 186 (1999) 215.

[43] J.W. Niemantsverdriet, A.M. van der Kraan, W.L. van Dijk, H.S. van der Baan, J. Phys. Chem. 54 (1980) 3363.

[44] C.N. Satterfield, R.T. Hanlon, S.E. Tung, Z. Zou, G.C. Papaefthymiou, Ind. Eng. Chem. Prod. Res. Dev. 25 (1986) 401.

[45] F. Tihay, A.C. Roger, G. Pourroy, A. Kiennemann, Energy Fuels 16 (2002) 1271.

[46] O. Ducreux, J. Lynch, B. Rebours, M. Roy, P. Chaumette, Stud. Surf. Sci. Catal. 119 (1998) 125.